Geophysical Journal International

Geophys. J. Int. (2013) **193,** 238–251 doi: 10.1093/gji/ggs080

Time-lapse changes of *P*- and *S*-wave velocities and shear wave splitting in the first year after the 2011 Tohoku earthquake, Japan: shallow subsurface

Kaoru Sawazaki[1,2] and Roel Snieder[2]

[1]*National Research Institute for Earth Science and Disaster Prevention,* 3-1 *Tennodai, Tsukuba, Ibaraki,* 305-0006*, Japan. E-mail: sawa@bosai.go.jp*
[2]*Center for Wave Phenomena, Department of Geophysics, Colorado School of Mines,* 1500 *Illinois Street, Golden, Colorado,* 80401-1887*, USA*

Accepted 2012 November 20. Received 2012 November 20; in original form 2012 July 23

SUMMARY

We detect time-lapse changes in *P*- and *S*-wave velocities (hereafter, V_P and V_S, respectively) and shear wave splitting parameters associated with the 2011 Tohoku earthquake, Japan, at depths between 0 and 504 m. We estimate not only medium parameters but also the 95 per cent confidence interval of the estimated velocity change by applying a new least squares inversion scheme to the deconvolution analysis of KiK-net vertical array records. Up to 6 per cent V_S reduction is observed at more than half of the analysed KiK-net stations in northeastern Japan with over 95 per cent confidence in the first month after the main shock. There is a considerable correlation between the *S*-wave traveltime delay and the maximum horizontal dynamic strain (MDS) by the main shock motion when the strain exceeds 5×10^{-4} on the ground surface. This correlation is not clearly observed for MDS at the borehole bottom. On the contrary, V_P and shear wave splitting parameters do not show systematic changes after the Tohoku earthquake. These results indicate that the time-lapse change is concentrated near the ground surface, especially in loosely packed soil layers. We conclude that the behaviour of V_P, V_S and shear wave splitting parameters are explained by the generation of omnidirectional cracks near the ground surface and by the diffusion of water in the porous subsurface. Recovery of V_S should be related to healing of the crack which is proportional to the logarithm of the lapse time after the main shock and/or to decompaction after shaking.

Key words: Inverse theory; Downhole methods; Earthquake ground motions; Site effects.

GJI Seismology

1 INTRODUCTION

The 2011 Tohoku earthquake (M_W 9.0) was the fourth largest earthquake since the modern seismograph network had been installed. Many researchers have shown the coseismic slip distribution between the Pacific and North-American plate boundary and detected up to 50 m slip near the Japan trench (e.g. Koketsu *et al.* 2011). In addition, strong accelerations up to 2000 Gal have been widely recorded in northeastern Japan associated with the main shock ground motion (e.g. Furumura *et al.* 2011). Tremendous aftershock activity with various types of focal mechanisms and post-seismic slip with a cumulative M_W of 8.5 followed the main shock (e.g. Asano *et al.* 2011; Ozawa *et al.* 2012). From these observations, it is speculated that medium properties such as seismic wave velocities, anisotropy, intrinsic attenuation and scattering coefficient changed widely as a consequence of the Tohoku earthquake.

Some researchers have reported these changes of velocity and anisotropy associated with the Tohoku earthquake. The detection methods used in these studies include deconvolution, spectral ratio and auto- and/or cross-correlation analyses. Nakata & Snieder (2011) measured a reduction in *S*-wave velocity of 10 per cent after the main shock in northeastern Japan by applying deconvolution to KiK-net vertical array records. KiK-net is the nationwide strong-motion digital seismic network in Japan operated by National Research Institute for Earth Science and Disaster Prevention (NIED; Okada *et al.* 2004). Wu & Peng (in press) measured the peak frequency of spectral ratios of KiK-net records and detected its logarithmic recovery after the main shock. Takagi & Okada (2012) and Nakata & Snieder (2012b) examined the change in shear wave splitting parameters near the ground surface after the main shock. These studies were based on the cross-correlation and deconvolution methods, respectively, which were applied to records of KiK-net. Both studies reported widespread increases in anisotropy coefficient in northeastern Japan, but the former reports decreases too at considerable number of stations. Using the autocorrelation function of ambient noise records registered by Hi-net (High-sensitivity seismograph network in Japan operated by NIED), Minato *et al.* (2012) detected a velocity reduction up to 1.5 per cent in northeastern Japan.

The reported time-lapse changes vary with employed methods because the different methods detect velocity changes at different depths. Because the deconvolution applied to a vertical array cancels out the source process and medium properties below the borehole receiver, the velocity reduction detected by this method represents change in the medium between the two receivers. The interpretation of time-lapse changes from the ambient noise-correlation method is more difficult because body and surface waves in a noise-correlated record have sensitivities to velocity change at different depths (Obermann *et al.* in press). Assuming a dominance of Rayleigh wave in 0.25–0.5 Hz ambient noise and taking the depth sensitivity kernel of the Rayleigh wave into account, Takagi *et al.* (2012) concluded that the velocity change near the ground surface after the 2008 Iwate-Miyagi Nairiku earthquake, Japan, is consistent with the change in phase velocity of the Rayleigh wave. Hobiger *et al.* (2012) applied the noise-correlation technique to the same earthquake in frequency ranges from 0.125 to 1.0 Hz and found a larger velocity reduction at the higher frequencies. These results indicate that the velocity change is concentrated near the ground surface up to a few hundred meters depth. Repeating earthquakes provide us with another constraint of the depth dependence. Applying coda wave interferometry to repeating earthquakes that occurred after the 2004 Parkfield earthquake, Rubinstein & Beroza (2005) pointed out that delays of *S*-coda wave are larger at the receivers on the ground surface than those in a borehole. It is important to combine these different methods to reveal the mechanism of the medium changes at different depths.

This paper documents the time-lapse changes of V_P, V_S and shear wave splitting parameters in the shallow subsurface up to 504 m depth after the Tohoku earthquake. We apply the deconvolution analysis developed by Nakata & Snieder (2012a) to KiK-net vertical array records. To examine the reliability of the estimated parameters quantitatively, we develop a least-squares inversion scheme and derive the 95 per cent confidence interval of the estimated changes. By comparing the obtained estimates with the observed strong motions, we evaluate the responsible depth for the medium changes. Finally, we interpret the mechanism of the time-lapse changes in these parameters using the theory of poroelasticity.

2 DATA

Each KiK-net station has two accelerometers; on the ground surface and at the borehole bottom. These accelerograms are sampled at 100 Hz with the dynamic range ±4000 Gal and by 24 bit resolution. The frequency response of the data acquisition system is flat from DC to about 20 Hz (Okada *et al.* 2004).

Fig. 1 shows KiK-net stations and earthquakes used for the deconvolution analysis. The number of stations used for the *S*- and *P*-wave analyses are 65 and 25, respectively, whereas 15 stations are used for both *S*- and *P*-wave analyses. The depth of the borehole receiver used in this study is distributed from 100 to 504 m for the *S*-wave analysis and from 150 to 1300 m for the *P*-wave analysis. We calculate the one-way traveltime of *P* and *S* waves between the surface and the borehole receivers by using well-log data provided by NIED, and exclude stations with a traveltime shorter than 0.08 s because peak shifts cannot be resolved for such small traveltimes. Because the traveltime of *P* wave is shorter than that of *S* wave, the number of available stations for the *P*-wave analysis is smaller than those for the *S*-wave analysis. Also, we exclude the stations which do not show a clear peak in the deconvolved waveforms.

We use earthquakes occurring between 2008 November 1 and 2012 March 11 (1 yr after the Tohoku earthquake), where the magnitude of the events ranged from 3.1 to 6.0. There are no inland earthquakes with $M_{\rm W}$ over 6 in northeastern Japan in the period from 2008 November 1 to 2011 March 11 (the date of the Tohoku earthquake), which certifies that significant long-term medium changes are not contaminated in the records before the Tohoku earthquake. To avoid non-linear site effect excited by a strong ground motion, we exclude the records with a maximum dynamic strain (MDS) exceeding 10^{-4}. Here, MDS is defined by $v_{{\rm max}S}/V_{S30}$, where $v_{{\rm max}S}$ and V_{S30} are the peak horizontal ground velocity recorded on the ground surface and the *S*-wave velocity averaged over top 30 m of soil (Borcherdt 1994; Takagi & Okada 2012), respectively. The threshold of 10^{-4} has been proposed in previous studies (e.g. Beresnev & Wen 1996). The focal depths of the used earthquakes are more than 40 km because seismic wave must be near vertically incident at the KiK-net borehole receiver.

3 METHOD

We suppose that a seismic wave propagates vertically from the KiK-net borehole bottom receiver to the surface. Under this assumption, a three component seismogram on the ground surface (S_E, S_N, S_Z) deconvolved by that at the borehole bottom (B_E, B_N, B_Z) gives the response function from the borehole bottom to the surface (Mehta *et al.* 2007). Therefore, the peak arrival time of the deconvolution approximately represents the traveltime between the two receivers. Nakata & Snieder (2012a) extended this method to a weakly anisotropic medium by using Alford rotation (Alford 1986). On the basis of the method of Nakata & Snieder (2012a), we develop a least squares inversion scheme to estimate V_P, V_S and shear wave splitting parameters.

3.1 *P*-wave analysis

For the analysis of V_P, we calculate the deconvolution $D_{P,i}$ by using the vertical component of the *i*th earthquake record as

$$D_{P,i}(t) = {\rm IFT}\left[\frac{\left\langle S_{Z,i}(\omega)\, B^{*}_{Z,i}(\omega)\right\rangle}{\left\langle \left|B_{Z,i}(\omega)\right|^{2}\right\rangle}\cdot W(\omega)\right], \tag{1}$$

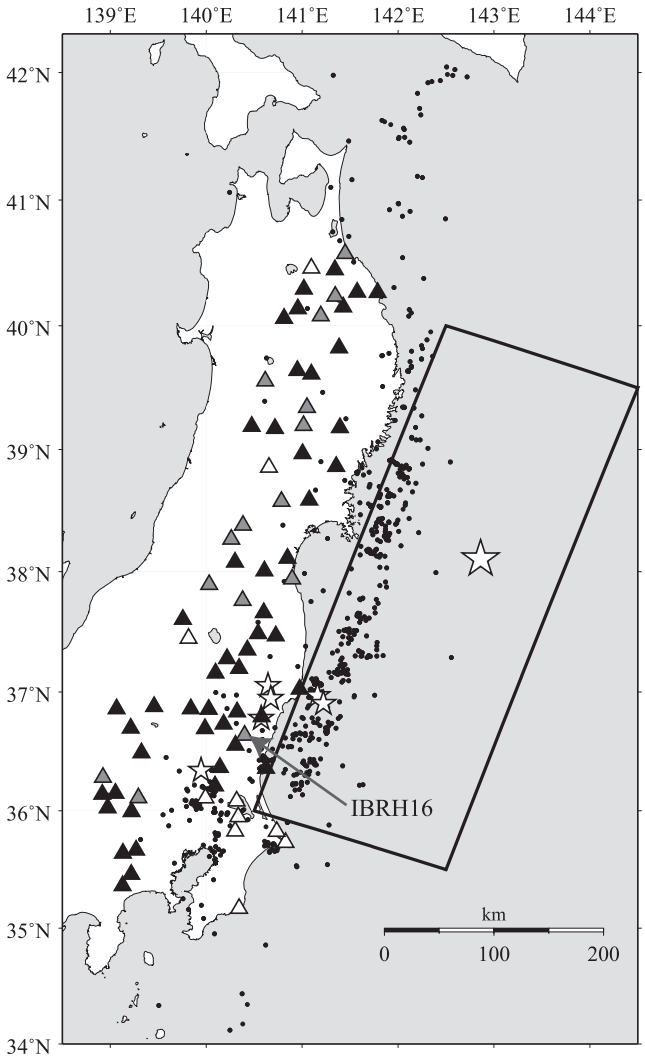

Figure 1. Map of the used KiK-net stations (triangles) and earthquakes (solid circles). The black, white and gray triangles are the stations used for S-wave, *P* wave and both S- and *P*-wave analyses, respectively. The rectangle indicates the approximate source area of the 2011 Tohoku earthquake. Large star indicates the location of the rupture onset of the Tohoku earthquake. Small stars indicate the epicenters of the earthquakes that excited the dynamic strain over 5×10^{-4} at least at one KiK-net station in the period from 1 to 12 months after the main shock. The location of station IBRH16, which is often referred in the text, is indicated by an arrow.

where ω and t represent angular frequency and lag time, respectively. The subscript Z represents a vertical component. The brackets $\langle\rangle$ denote an application of a Hanning window to stabilize the deconvolution (Sawazaki *et al.* 2009). $W(\omega)$ is a 1–10 Hz bandpass filter and IFT represents inverse Fourier transform. Fig. 2 shows the time windows used for the deconvolution. The time window of *P* wave begins from the *P*-wave picking time of the vertical component and is 10.24 s long.

The average of the deconvolved waveforms is calculated using all the earthquakes occurred in each time period before the main shock (from 2008 November 1 to 2011 March 11), from 0 to 1 month, from 1 to 3 months, from 3 to 6 months and from 6 to 12 months after the main shock. The averaged deconvolution $\overline{D}_{P,T}$ and the variance of the average $\sigma^2_{\overline{D}P,T}$ in the time period T are given by

$$\overline{D}_{P,T}(t) = \frac{1}{N_T}\sum_{i=1}^{N_T} D_{P,i}(t), \tag{2}$$

and

$$\sigma^2_{\overline{D}P,T}(t) = \frac{1}{N_T^2}\sum_{i=1}^{N_T}\left[D_{P,i}(t) - \overline{D}_{P,T}(t)\right]^2, \tag{3}$$

respectively, where N_T is the number of used earthquakes in the time period T. Note that $\sigma^2_{\overline{D}P,T}$ is not the variance of $D_{P,i}$ but is the variance of $\overline{D}_{P,T}$ which is derived from a central limit theorem (Bevington & Robinson 1992). Hereafter, we omit the subscript T for simplicity.

The peak arrival time of the deconvolution is calculated by fitting a quadratic function $y(t) = at^2 + bt + c$ to the sequence of discrete deconvolution amplitudes $\overline{D}_P(t_{\max} - \Delta t)$, $\overline{D}_P(t_{\max})$ and $\overline{D}_P(t_{\max} + \Delta t)$, where $t_{\max}$ and Δt are the lag time which gives the maximum

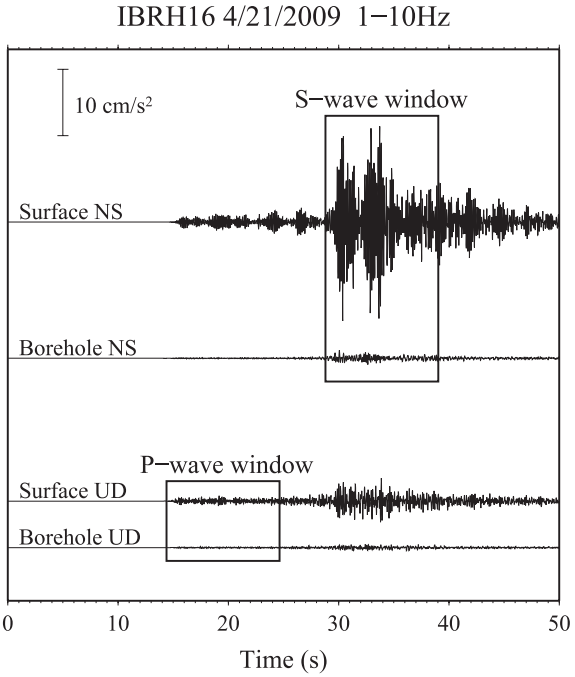

Figure 2. NS and UD components of the 1–10 Hz accelerograms recorded on the ground surface and at the borehole bottom of the KiK-net station IBRH16 for the earthquake of 2009 April 21. The rectangles are the *P*- and *S*-wave time windows used for the deconvolution analysis. The origin time is beginning of the record, not the onset time of the earthquake. The scale of acceleration is common for all the traces.

amplitude of $\overline{D}_P$ and the time sampling interval (0.01 s for the KiK-net system), respectively. Note that we do not apply a stretching method (Hadziioannou *et al.* 2009) to the coda of the deconvolved record because the number of data is so small that coda of the deconvolution is not stable. Hereafter, we denote the sequence of these three lag times by $t_- \equiv t_{\max} - \Delta t$, $t_0 \equiv t_{\max}$ and $t_+ \equiv t_{\max} + \Delta t$. The weighted least-squares solution (Menke 1989) for the coefficients of the quadrant function a, b and c is given by

$$\mathbf{M} \equiv \begin{bmatrix} a \\ b \\ c \end{bmatrix} = \left[\mathbf{G}^T \operatorname{cov}\mathbf{D}^{-1}\mathbf{G}\right]^{-1} \mathbf{G}^T \operatorname{cov}\mathbf{D}^{-1}\mathbf{D}$$

$$\operatorname{cov}\mathbf{M} \equiv \begin{pmatrix} \sigma_{aa}^2 & \sigma_{ab}^2 & \sigma_{ac}^2 \\ \sigma_{ba}^2 & \sigma_{bb}^2 & \sigma_{bc}^2 \\ \sigma_{ca}^2 & \sigma_{cb}^2 & \sigma_{cc}^2 \end{pmatrix} = \left[\mathbf{G}^T \operatorname{cov}\mathbf{D}^{-1}\mathbf{G}\right]^{-1}, \tag{4}$$

$$\mathbf{G} \equiv \begin{bmatrix} t_-^2 & t_- & 1 \\ t_0^2 & t_0 & 1 \\ t_+^2 & t_+ & 1 \end{bmatrix}, \mathbf{D} \equiv \begin{bmatrix} \bar{D}_P(t_-) \\ \bar{D}_P(t_0) \\ \bar{D}_P(t_+) \end{bmatrix}, \operatorname{cov}\mathbf{D} \equiv \begin{bmatrix} \sigma_{\overline{D}P,--}^2 & \sigma_{\overline{D}P,-0}^2 & \sigma_{\overline{D}P,-+}^2 \\ \sigma_{\overline{D}P,0-}^2 & \sigma_{\overline{D}P,00}^2 & \sigma_{\overline{D}P,0+}^2 \\ \sigma_{\overline{D}P,+-}^2 & \sigma_{\overline{D}P,+0}^2 & \sigma_{\overline{D}P,++}^2 \end{bmatrix}$$

where **M**, cov**M**, **G**, **D** and cov**D** represent model parameter vector, covariance matrix for the model parameters, kernel matrix, data vector and covariance matrix for the data, respectively.

In this inversion, the variance of the averaged deconvolution is mapped onto the uncertainty of the estimated parameters. Obviously, the non-diagonal components of cov**D** are not zero because the bandwidth of the applied bandpass filter $W(\omega)$ in eq. (1) is narrower than the Nyquist frequency 50 Hz. By taking the finite bandwidth into account, we define each component of cov**D** to be given by

$$\begin{aligned} \sigma_{\overline{D}P,--}^2 &\equiv \sigma_{\overline{D}P,00}^2 \equiv \sigma_{\overline{D}P,++}^2 \equiv \frac{1}{3}\left[\sigma_{\overline{D}P}^2(t_-) + \sigma_{\overline{D}P}^2(t_0) + \sigma_{\overline{D}P}^2(t_+)\right] \\ \sigma_{\overline{D}P,-0}^2 &\equiv \sigma_{\overline{D}P,0+}^2 \equiv \sigma_{\overline{D}P,0-}^2 \equiv \sigma_{\overline{D}P,+0}^2 \equiv \sigma_{\overline{D}P,00}^2 \exp\left[-\frac{\pi^2}{4}(f_H - f_L)^2 \Delta t^2\right] \cos\left[\pi(f_H + f_L)\Delta t\right], \\ \sigma_{\overline{D}P,-+}^2 &\equiv \sigma_{\overline{D}P,+-}^2 \equiv \sigma_{\overline{D}P,00}^2 \exp\left[-\pi^2(f_H - f_L)^2 \Delta t^2\right] \cos\left[2\pi(f_H + f_L)\Delta t\right] \end{aligned} \tag{5}$$

where $f_L = 1$ Hz and $f_H = 10$ Hz are the lower and upper band limit of the bandpass filter, respectively. See the Appendix for a derivation of the exponential and cosine terms in the non-diagonal components of eq. (5).

By solving the least-squares inversion given by eq. (4), we derive V_P and its variance $\sigma^2{}_{VP}$ as

$$V_P = -\frac{2a}{b}H \tag{6}$$

and

$$\sigma^2_{VP} = \left(\frac{\partial V_P}{\partial a}\right)^2 \sigma^2_{aa} + \left(\frac{\partial V_P}{\partial b}\right)^2 \sigma^2_{bb} + 2\left(\frac{\partial V_P}{\partial a}\right)\left(\frac{\partial V_P}{\partial b}\right)\sigma^2_{ab} = V_P^2\left[\frac{1}{a^2}\sigma^2_{aa} + \frac{1}{b^2}\sigma^2_{bb} - \frac{2}{ab}\sigma^2_{ab}\right], \tag{7}$$

respectively, where H is the distance between the two receivers. For the derivation of eq. (7), we use the principle of error propagation (Bevington & Robinson 1992).

3.2 *S*-wave analysis

Before the analysis of *Vs* and shear wave splitting parameters, we correct the polarization of two horizontal components at the borehole bottom receiver using the rotation angle provided by NIED (Shiomi *et al.* 2003). We calculate the deconvolved waveforms $D_{S,i}$ by using two horizontal components at each KiK-net station as

$$\begin{aligned} D_{S,i}\left(t,\phi_j\right) &= IFT\left[\frac{\left\langle S_i\left(\omega,\phi_j\right)B_i^*\left(\omega,\phi_j\right)\right\rangle}{\left\langle\left|B_i\left(\omega,\phi_j\right)\right|^2\right\rangle}\cdot W(\omega)\right] \\ S_i\left(\omega,\phi_j\right) &\equiv S_{E,i}(\omega)\cos\phi_j + S_{N,i}(\omega)\sin\phi_j \\ B_i\left(\omega,\phi_j\right) &\equiv B_{E,i}(\omega)\cos\phi_j + B_{N,i}(\omega)\sin\phi_j, \end{aligned} \tag{8}$$

where ϕ_j is the polarization azimuth of the horizontal component measured from 0 degree (east) to 180 degree (west) in 10 degree interval. As a result, we obtain $J = 18$ deconvolved traces for each earthquake–station pair. The time window used for the deconvolution begins from the *S*-wave picking time of the horizontal component and is 10.24 s long (see Fig. 2). We do not use the late *S*-wave coda in this study because the waves comprising the *S*-coda propagates in all possible directions and with different polarizations, which is not appropriate for shear wave splitting analysis. We apply equations from (2) through (7) to $D_{S,i}(t,\phi_j)$ to derive $V_S(\phi_j)$ and its variance $\sigma^2{}_{VS}(\phi_j)$ for each polarization azimuth. The time periods used for the averaging are the same as those used for the *P*-wave analysis.

When an *S* wave is incident vertically to an anisotropic medium which gives a shear wave splitting, the *S*-wave velocity from the borehole bottom to the surface has an azimuthal periodicity given by

$$V_S\left(\phi_j\right) = v_0 + v_1\cos 2\phi_j + v_2\sin 2\phi_j \tag{9}$$

(Alford 1986). This formulation is valid if the anisotropy is weak and the splitting time is much shorter than the dominant period of the deconvolved waveform (Nakata & Snieder 2012a). The weighted least-squares solution for the coefficients v_0, v_1 and v_2 is given by

$$\mathbf{M} \equiv \begin{bmatrix} v_0 \\ v_1 \\ v_2 \end{bmatrix} = \left[\mathbf{G}^T \mathrm{cov}\mathbf{D}^{-1}\mathbf{G}\right]^{-1}\mathbf{G}^T\mathrm{cov}\mathbf{D}^{-1}\mathbf{D}$$

$$\mathrm{cov}\mathbf{M}' \equiv \begin{pmatrix} \sigma^{2'}_{v00} & \sigma^{2'}_{v01} & \sigma^{2'}_{v02} \\ \sigma^{2'}_{v10} & \sigma^{2'}_{v11} & \sigma^{2'}_{v12} \\ \sigma^{2'}_{v20} & \sigma^{2'}_{v21} & \sigma^{2'}_{v22} \end{pmatrix} = \left[\mathbf{G}^T\mathrm{cov}\mathbf{D}^{-1}\mathbf{G}\right]^{-1}$$

$$\mathbf{G} \equiv \begin{bmatrix} 1 & \cos 2\phi_1 & \sin 2\phi_1 \\ 1 & \cos 2\phi_2 & \sin 2\phi_2 \\ \vdots & \vdots & \vdots \\ 1 & \cos 2\phi_J & \sin 2\phi_J \end{bmatrix}, \mathbf{D} \equiv \begin{bmatrix} V_S(\phi_1) \\ V_S(\phi_2) \\ \vdots \\ V_S(\phi_J) \end{bmatrix}, \mathrm{cov}\mathbf{D} \equiv \begin{bmatrix} \sigma^2_{VS,11} & \sigma^2_{VS,12} & \cdots & \sigma^2_{VS,1J} \\ \sigma^2_{VS,21} & \sigma^2_{VS,22} & \cdots & \sigma^2_{VS,2J} \\ \vdots & \vdots & \ddots & \vdots \\ \sigma^2_{VS,J1} & \sigma^2_{VS,J2} & \cdots & \sigma^2_{VS.JJ} \end{bmatrix}. \tag{10}$$

Because we do not know a-priori functional form of the covariance component of cov**D**, we assume each component of cov**D** to be given by

$$\sigma^2_{VS,jk} \equiv \sigma^2_{VS}\left(\phi_j\right)\delta_{jk}, \tag{11}$$

where δ_{jk} is Kronecker delta. Note that the error of the estimated parameters must be independent from the choice of the sampling interval of ϕ_j because each $V_S(\phi_j)$ is calculated by rotating only two independent components (EW and NS). Therefore, we modify cov$\mathbf{M}'$ in eq. (10) as

$$\mathrm{cov}\mathbf{M} \equiv \begin{pmatrix} \sigma_{v00}^2 & \sigma_{v01}^2 & \sigma_{v02}^2 \\ \sigma_{v10}^2 & \sigma_{v11}^2 & \sigma_{v12}^2 \\ \sigma_{v20}^2 & \sigma_{v21}^2 & \sigma_{v22}^2 \end{pmatrix} = \frac{\sigma_{VS,E}^2 + \sigma_{VS,N}^2}{4\sigma_{v00}^{2'}} \mathrm{cov}\mathbf{M}' \tag{12}$$

$$\sigma_{VS,E}^2 \equiv \sigma_{VS}^2(\phi = 0), \sigma_{VS,N}^2 \equiv \sigma_{VS}^2(\phi = \pi/2),$$

where the regularization factor $\sigma_{v00}^2 = \left(\sigma_{VS,E}^2 + \sigma_{VS,N}^2\right)/4$ is the variance of v_0 obtained when only EW and NS components are used for the estimation of v_0. We verified that cov$\mathbf{M}$ defined by eq. (12) does not vary with the choice of the sampling interval of ϕ_j.

From the least-squares solution of eq. (10), we derive the average *S*-wave velocity V_S, the anisotropy coefficient AC and the fast V_S direction ψ as

$$V_S \equiv v_0, AC \equiv 2\sqrt{v_1^2 + v_2^2}, \psi \equiv \frac{1}{2}\tan^{-1}\left(\frac{v_2}{v_1}\right). \tag{13}$$

Their variances $\sigma^2{}_{VS}$, $\sigma^2{}_{AC}$, $\sigma^2{}_{\psi}$ and the covariance $\sigma^2{}_{AC\psi}$ are given by

$$\begin{aligned} \sigma_{VS}^2 &= \sigma_{v00}^2 \\ \sigma_{AC}^2 &= \frac{16}{AC^2}\left(v_1^2\sigma_{v11}^2 + v_2^2\sigma_{v22}^2 + 2v_1v_2\sigma_{v12}^2\right) \\ \sigma_{\psi}^2 &= \frac{4}{AC^4}\left(v_2^2\sigma_{v11}^2 + v_1^2\sigma_{v22}^2 - 2v_1v_2\sigma_{v12}^2\right) \\ \sigma_{AC\psi}^2 &= \frac{8}{AC^3}\left[-v_1v_2\sigma_{v11}^2 + v_1v_2\sigma_{v22}^2 + \left(v_1^2 - v_2^2\right)\sigma_{v12}^2\right]. \end{aligned} \tag{14}$$

The 95 per cent confidence interval of the true model parameter M_t around the estimated parameter M is given by

$$M - 1.96\sqrt{\sigma_M^2} \le M_t \le M + 1.96\sqrt{\sigma_M^2}, \tag{15}$$

where the factor 1.96 arises from the 95 per cent confidence region of the standard normal distribution (Aster *et al.* 2011). Using eq. (15), we estimate the 95 per cent confidence interval for all the parameters V_P, V_S, AC and ψ. A 95 per cent confidence ellipse of the shear wave splitting parameters in a spherical coordinate system with radius AC and polar angle ψ is given by

$$\frac{1}{A^2\left[\sigma_{AC}^2\sigma_{\psi}^2 - \left(\sigma_{AC\psi}^2\right)^2\right]} \left\{ \begin{aligned} &A^2\sigma_{\psi}^2\left[AC_t\cos(\psi_t - \psi) - AC\right]^2 \\ &-2AA_t\sigma_{AC\psi}^2\left[AC_t\cos(\psi_t - \psi) - AC\right]\sin(\psi_t - \psi) \\ &+A_t^2\sigma_{AC}^2\sin^2(\psi_t - \psi) \end{aligned} \right\} \le 5.99, \tag{16}$$

where the factor 5.99 is the 95 per cent percentile of the χ^2 distribution with two degrees of freedom (Aster *et al.* 2011).

4 TIME-LAPSE CHANGES AND THEIR UNCERTAINTIES

4.1 Possible bias caused by incident angle

To check the incident angle of the used seismic waves, we apply 1-D ray tracing to each source-station pair by using the 1-D velocity structure provided by Nakajima *et al.* (2001). Most of the measured incident angles are less than 30 degrees at the borehole bottom receivers.

Using the obtained incident angles and well-log data provided by NIED, we further synthesize *SH*-, *SV*- and *P*-wave deconvolution waveforms for all the source-station pairs. The synthetic response functions for layered media are calculated on the basis of the propagator matrix method by Silva (1976). The inverse of the quality factor Q^{-1} is set to 0.05 for both *S*- and *P* waves for all frequencies. The mass density ρ (kg/m^3) is set to $\rho = 310V_P^{0.25}$ according to Gardner *et al.* (1974). In Fig. 3(a), we show the average (thick curves) and the 95 per cent confidence interval (thin curves) of the synthesized deconvolution waveforms at station IBRH16 in the periods before (black) and from 0 to 1 month after (gray) the main shock. The velocity profile used for the syntheses is shown in Fig. 4. The arrows and numerals indicate the peak arrival time and its 95 per cent confidence interval estimated by the least squares inversion method explained in Chapter 3. Note that the thin curves almost overlap with the thick curves because the confidence intervals are very small.

There are differences up to 0.6 per cent between the peak arrival times before and after the main shock for all *SH*-, *SV*- and *P*-wave deconvolutions. Because the used velocity profile is the same for both time periods, this difference indicates a possible bias originated from changes in the incidence angles in the two periods. There is another slight difference up to 0.2 per cent between the peak arrival times of *SH*- and *SV*-wave deconvolutions. This difference is an artificial anisotropy originated from non-vertical incidences to a layered isotropic medium. Even though the velocity structure does not change and anisotropy does not exist, the observed deconvolution can include these biases, which causes uncertainty of the estimation.

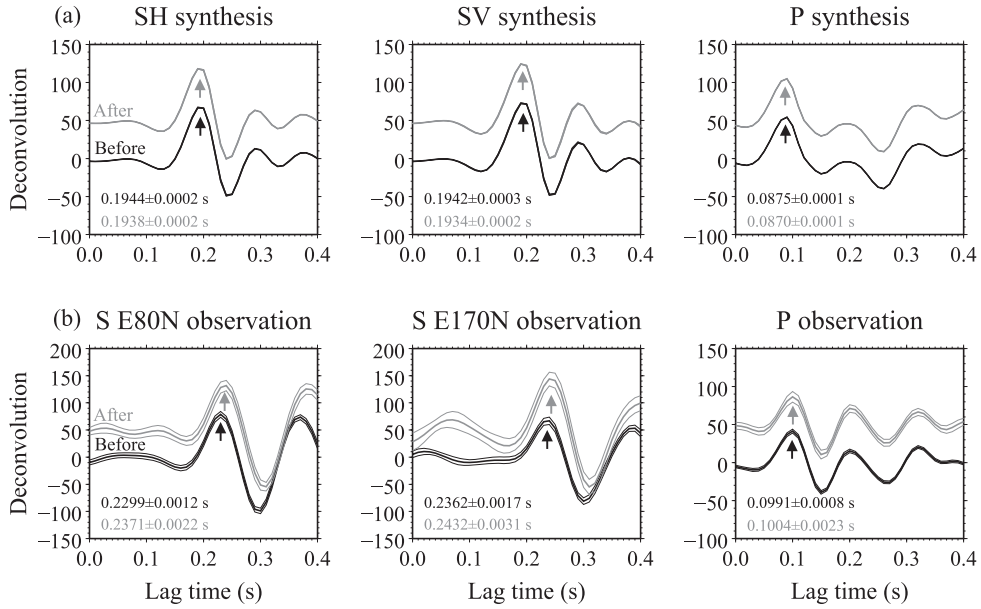

Figure 3. (a) Synthesized deconvolution waveforms for the horizontal component of *SH* and *SV* waves and for the vertical component of *P* wave calculated from the well-log data of station IBRH16 (Fig. 4). (b) Observed deconvolution waveforms for the horizontal components of *S*-wave polarized to E80N and E170N and for the vertical component of *P* wave at station IBRH16. The gray and black curves represent the deconvolutions in the period before and from 0 to 1 month after the main shock, respectively. The latter is shifted to upperward by 50 in amplitude scale. The thick and thin curves represent the average and the 95 per cent confidence interval of the deconvolution, respectively. The arrows and numerals indicate the peak arrival times with the 95 per cent confidence interval.

These biases are, however, much smaller than the observed changes. For comparison, we show the average and the 95 per cent confidence interval of the observed deconvolution waveforms for *S* and *P* waves at the same station and the same time periods in Fig. 3(b). Note that because the velocity profile of well-log data used for the syntheses and the true velocity structure are different (see fig. 8 of Nakata & Snieder 2012a), the peak arrival times of the observed deconvolutions differ from the synthesized counterparts within 20 per cent for both *S* and *P* waves. Nevertheless, this difference is not crucial for the estimation of velocity changes.

The difference between the peak arrival times before and after the main shock is more than 3 per cent for the observed *S*-wave deconvolutions. Because this difference is much larger than the possible bias originated from the distribution of incidence angle, we conclude that the observed change is mainly caused by change of the *S*-wave velocity. The difference up to 3 per cent is also found between the peak arrival times of *S*-wave deconvolutions polarized at 80 degrees and 170 degrees. Because this difference is also much larger than the artificial anisotropy originated from the difference of *SH* and *SV* deconvolutions, we conclude that most of the observed shear wave splitting are not artificial, but is because of the anisotropy structure in the medium.

Following these results, we conclude that a bias caused by the distribution of incident angle does not affect the estimation of the medium parameters significantly.

4.2 Estimated parameters

Fig. 5 shows time-lapse changes of normalized V_S (black) and V_P (gray) at station IBRH16. The left panel shows the 95 per cent confidence interval of the background velocities before the main shock. The right panel shows time-lapse change in the velocities after the main shock (thick lines) and the 95 per cent confidence interval (thin lines). Note that all the velocities are normalized by the values obtained before the main shock, thus the estimated values before the main shock are equal to 1 by definition. The lapse time is shown in the right panel on a logarithmic scale.

V_S is reduced by 3 per cent in the first month after the main shock, which is far beyond the 95 per cent confidence interval. V_S continues to recover for 1 yr proportional to the logarithm of the lapse time. On the other hand, the reduction of V_P is much smaller than that of V_S in the same period. The confidence interval of V_P is so large that any reduction of V_P cannot be inferred with any statistical significance.

Fig. 6 shows estimations of the shear wave splitting parameters (circles) and 95 per cent confidence ellipses at station IBRH16. The radius and polar angle represent AC normalized by V_S and ψ, respectively. Different colours represent different time periods. Note that ψ has a 180 degree ambiguity because of eq. (9). There is no systematic change in the shear wave splitting parameters between the periods before and from 0 to 1 month after the main shock; the black and red error ellipses almost overlap. AC decreases in the period from 1 to 3 months after the main shock, but the error ellipses still largely overlap. In the periods from 3 to 12 months after the main shock, the shear wave splitting parameters mostly return to the original values. We checked that station IBRH16 did not experience ground motion as strong as the main shock motion in the period from 1 to 3 months after the main shock, which suggests that the changes of the shear wave splitting parameters are not influenced by strong ground motion.

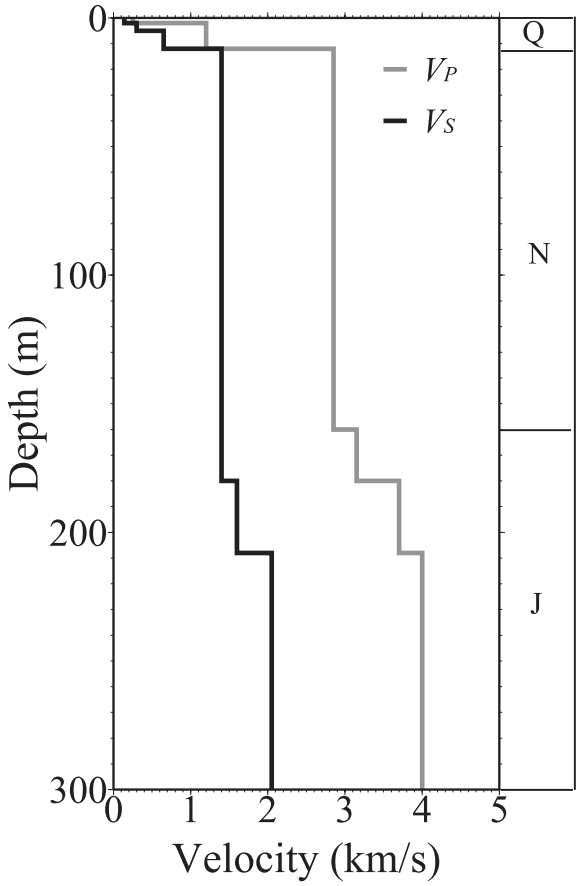

Figure 4. Well-log data of V_P and V_S at station IBRH16 with the geological age. The marks Q, N and J represent Quaternary, Neogene and Jurassic periods, respectively. The top 12 m layers consist of sandy gravel. The layers from 12 to 134 m depths are a mixture of tuff, sandstone and siltstone. The layers deeper than 134 m are composed of sandstone.

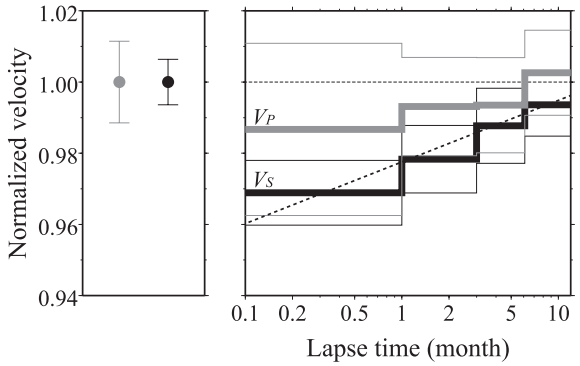

Figure 5. Time-lapse changes in V_S (thick black line) and V_P (thick gray line) after the 2011 Tohoku earthquake at station IBRH16. The velocities are normalized by the values estimated before the main shock as shown in the left panel. The error bars in the left panel and thin lines in the right panel represent the 95 per cent confidence interval. The black broken line represents the regression line for the normalized V_S.

Applying Student's t test to the parameters V_P, V_S, AC and ψ estimated before and from 0 to 1 month after the main shock, we count number of stations which are responsible for the changes of these parameters with more than 95 per cent confidence. The result is summarized in Table 1. The numerator and denominator represent the number of stations with a change more than 95 per cent confidence and the total number of used stations, respectively. From this table, we conclude that changes of V_P, AC and ψ are under the detection level in this study. Only a reduction in V_S is observed beyond 95 per cent confidence for more than half of the used stations. This result does not mean V_P, AC and ψ do not change after the main shock, but it means we need more data and better data selection to confirm the changes in these parameters with more than 95 per cent confidence.

Fig. 7 shows maps of (1) V_S and (2) V_P normalized by the values obtained before the main shock, (3) change of AC/V_S after the main

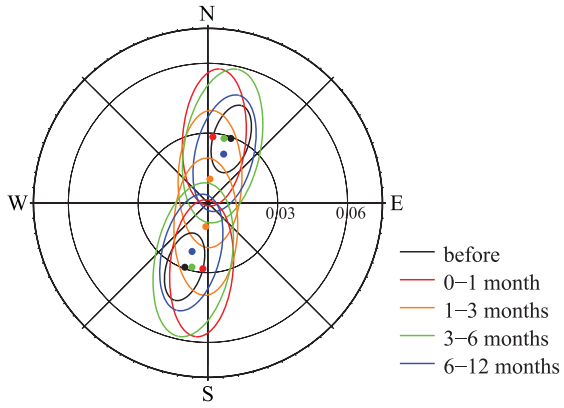

Figure 6. Estimated shear wave splitting parameters in the time periods before the main shock (black), from 0 to 1 month (red), from 1 to 3 months (orange), from 3 to 6 months (green) and from 6 to 12 months (blue) after the main shock at station IBRH16. The radius and polar-angle represent AC/V_S and ψ, respectively. The solid circles and ellipses are the estimated values and the area of 95 per cent confidence, respectively. Because the azimuthal dependence has 180 degree ambiguity according to eq. (9), the figure is drawn as the origin point reflection.

Table 1. Number of stations responsible for the change of parameters with more than 95 per cent confidence in the first month after the main shock.

	V_P	V_S	AC	ψ
Increase	2/25	2/65	3/65	5/65
Decrease	3/25	37/65	0/65	

shock and (4) ψ in each time period. Note that the used colour scales are the same for Figs 7(a)–(c). The black and red arrows in Fig. 7(d) represent ψ before and after the main shock, respectively. The results are shown for all the used stations regardless their confidence interval.

Vs decreases up to 6 per cent in the first month after the main shock. Especially large reductions are observed at the stations which experienced stronger ground motion by the main shock (see fig. 2 of Furumura *et al.* 2011). Many stations in the northern part of the target area show a complete recovery within 1 yr, whereas the recovery takes more time at many stations at the southern part. In Fig. 1, we mark the locations of aftershocks and/or triggered earthquakes which excited a dynamic strain exceeding 5×10^{-4} at least at one KiK-net station by small stars. Because the location is concentrated at southern part of the target area, we infer that cumulative damage by aftershocks and/or triggered earthquakes may extend the apparent recovery time. Some studies pointed out that rocks suffered by strong motions become more susceptive to the additional strong motions (e.g. Rubinstein & Beroza 2004), which supports our finding. On the contrary, about half of the used stations show increase in V_P in the first month after the main shock. The amount of change is within 2 per cent at most stations. The time-lapse recovery of V_P is much less clear than that of V_S.

For the shear wave splitting parameters, we observe both increase and decrease in AC/V_S in the first month after the main shock. The amount of change is less than 4 per cent at most stations, which is not as large as that of V_S. Also, the regional pattern and time-lapse recovery of AC are not as clear as those of V_S. The fast V_S direction does not change through the time periods at most stations, and it does not show a clear spatial pattern.

5 DISCUSSION

5.1 Strong motion and changes in V_S and shear wave splitting parameters

In Fig. 8, we show a correlogram between MDS by the main shock ground motion and the *S*-wave traveltime delay in the first month after the main shock using all 65 stations used for the *S*-wave analysis. The definition of MDS on the ground surface (Fig. 8a) is the same as that explained in Chapter 2. The definition of MDS at the borehole receiver (Fig. 8b) is $v_{\mathrm{max}B}/V_{SB}$, where $v_{\mathrm{max}B}$ and V_{SB} are the peak horizontal ground velocity at the borehole bottom and the *S*-wave velocity at the borehole receiver, respectively. We note that the peak ground acceleration, which is often used as an index of the strength of the ground motion, is not used here because MDS has a better correlation with the traveltime delay (Takagi & Okada 2012). The *S*-wave traveltime delay is used instead of V_S change ratio because the delay is not affected by the traveltime between two receivers.

On the ground surface, there is a considerable positive correlation (correlation coefficient = 0.58) especially when MDS exceeds about 5×10^{-4} (white zone). Note that the threshold value 5×10^{-4} is much larger than 10^{-4}, the excitation threshold of non-linear site response (see Chapter 2). In contrast, MDS at the borehole bottom receiver does not exceed 5×10^{-4} at most stations, and does not correlate well with the *S*-wave traveltime delay (correlation coefficient = 0.34). Consequently, we speculate that the V_S change is concentrated near the ground

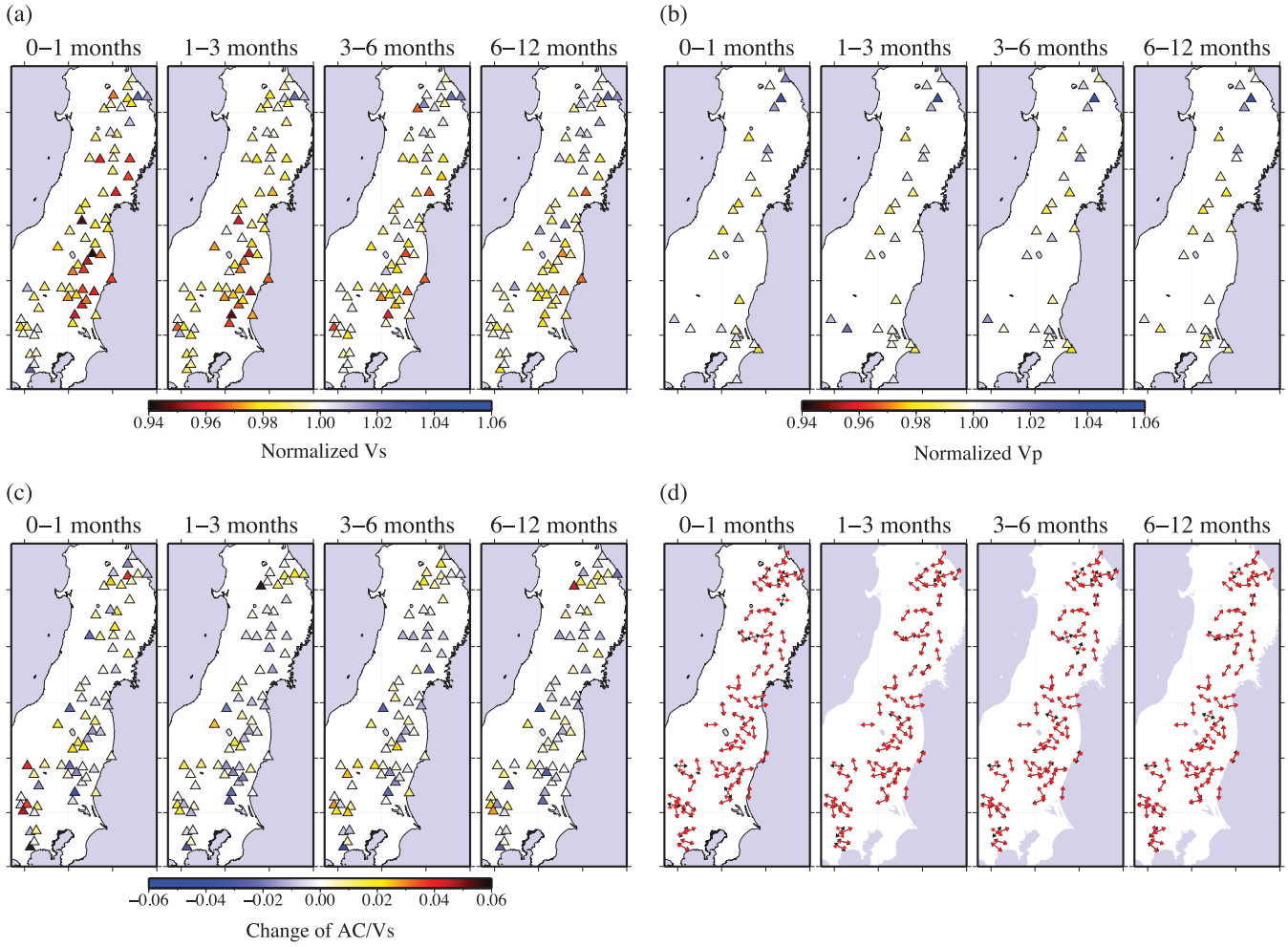

Figure 7. Map of (a) V_S, (b) V_P, (c) change of AC/V_S and (d) ψ in each time period. The velocities of (a) and (b) are normalized by the values that estimated before the main shock. Black and red arrows of (d) indicate the results before and after the main shock, respectively.

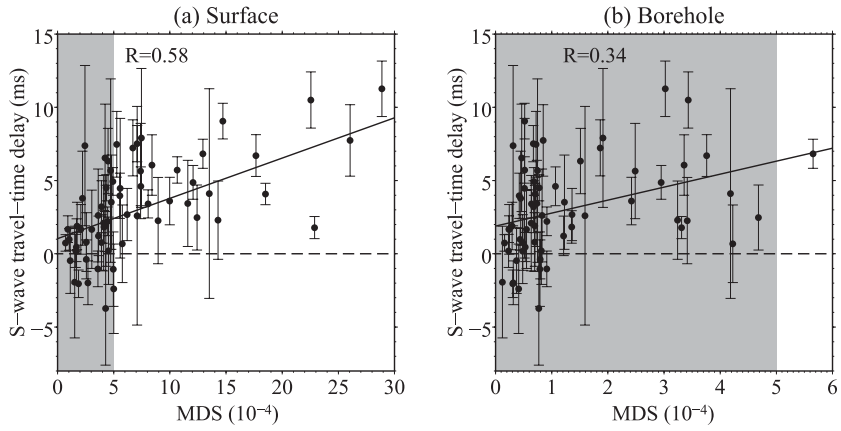

Figure 8. Correlogram of *S*-wave travel time delay in the first month after the main shock versus MDS by the main shock motion recorded (a) on the ground surface and (b) at the borehole bottom. The shaded area corresponds to the MDS less than 5×10^{-4}. The black lines and R are the regression line and the correlation coefficient, respectively.

surface, where the MDS is much larger than it is at greater depth. According to the well-log data of station IBRH16 (Fig. 4), the layers in the upper 12 m are composed of young sandy gravel. This suggests that the strong motion amplified at the weak, shallowest layers caused the reduction of V_S.

On the other hand, the strong motion does not always cause a change in the shear wave splitting parameters. Fig. 9 shows the azimuthal dependence of MDS by the main shock motion on the ground surface at station IBRH16. Because no clear directionality is observed in the MDS, there are no reasons why the cracks in the top layers generated by the main shock motion have a specific orientation. We note that there

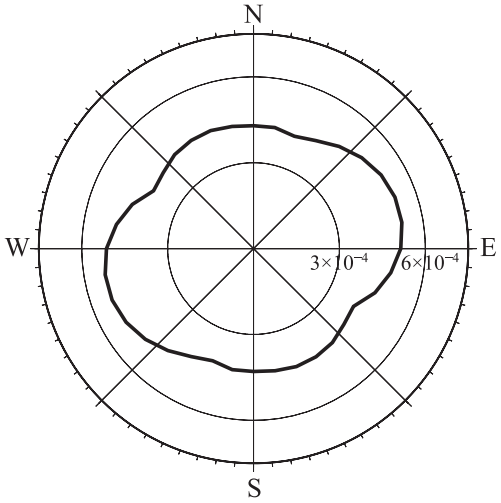

Figure 9. Azimuthal dependence of the horizontal MDS by the main shock motion on the ground surface at station IBRH16. The radius and polar angle represent the MDS and the polarization azimuth, respectively.

is no correlation between MDS and the amount of change in AC/V_S (see Fig. 7c), which confirms that strong motion is not the main cause of the changes in the shear wave splitting parameters.

In contrast, a static strain change is associated with a specific orientation. Nakata & Snieder (2012a) found a clear correlation between the fast shear wave velocity direction and the tectonic stress direction at the deep boreholes. Consequently, if the static strain change by the coseismic crustal deformation is significant at relatively deeper part of the borehole, it can change the shear wave splitting parameters. Because we do not observe clear changes in these parameters, we conclude that the static strain change is not the primary cause of the medium changes at depths less than 504 m, the depth of the deepest borehole station in this study.

Our result on shear wave splitting parameters seems to differ from that of Nakata & Snieder (2012b) who widely observed increase of AC in northeastern Japan. This discrepancy is explained as follows. Nakata & Snieder (2012b) calculated the average of AC for all the earthquakes occurring in each time period. On the other hand, we first calculate average of the deconvolutions for all the earthquakes that occurred in each period, and then calculate AC and ψ of the 'averaged' deconvolution. Therefore, our estimation is the vector average of the shear wave splitting parameters, which always has smaller amplitude than the scalar average used by Nakata & Snieder (2012b). Because the variance of ψ after the main shock tends to be larger than that before the main shock, the vector average tends to have smaller amplitudes after the main shock, which may be one of the reasons why we do not detect systematic increase in AC after the main shock.

5.2 Interpretation of time-lapse changes based on rock physics

We found that changes of V_P are smaller than those of V_S at most of the stations. To explain this result, we use the theory of poroelasticity. According to Gassmann (1951) and Walsh (1965), bulk modulus K, shear modulus μ and mass density ρ in a porous medium are given by

$$\begin{aligned} K_{dry} &= K_S\left(1-\beta\frac{\phi}{A}\right) K_{sat} = K_{dry} + \frac{K_w\left(1-K_{dry}/K_S\right)^2}{\phi + \left(1-\phi-K_{dry}/K_S\right)K_w/K_S} \\ \mu_{dry} &= \mu_S\left(1-\beta'\frac{\phi}{A}\right)\mu_{sat} = \mu_{dry} \\ \rho_{dry} &= \rho_S(1-\phi)\,\rho_{sat} = \rho_S(1-\phi) + \rho_w\phi \end{aligned} \quad , \tag{17}$$

where the subscripts '*dry*' and '*sat*' represent the values of unsaturated and saturated porous medium, respectively. Subscripts '*S*', and '*w*' indicate properties of solid material part and water part which construct the porous medium, respectively. ϕ and A are porosity and aspect ratio of spheroidal cracks in the medium which satisfy $\phi \ll 1$ and $\phi < A < 1$, respectively. β and β' are constants which are approximately equal to 1. Eq. (17) is summarized in table 7.4 of Gueguen & Palciauskas (1994).

The aspect ratio of cracks decreases when cracks are grown by strong ground motion. Also, increase of percolation by the crack growth accelerates the diffusion of groundwater, which may saturate the porous vadose zone. Actually, there are reports on widespread liquefaction after the Tohoku Earthquake especially around Tokyo Bay and Tone River (e.g. Bhattacharya *et al.* 2011). Because decrease of the aspect ratio decreases μ and the water saturation increases ρ according to eq. (17), V_S always decreases because of the relation $V_S = \sqrt{\mu/\rho}$. However, because the water saturation increases K, V_P defined by $V_P = \sqrt{\left(K+4/3\mu\right)/\rho}$ can increase under certain conditions. This idea supports the observed increases in V_P shown in Fig. 7(b).

We note that this idea is valid only for a medium with small porosity ($\phi \ll 1$), which is not always the case in the shallow ground. According to Blatt (1979), the average value of ϕ obtained from well-log cores at the depth of a few hundred meters is 0.3–0.4 for sandstone. For an unconsolidated large ϕ medium, increase of pore fluid pressure reduces its shear modulus, which is not considered in the above discussion. Nevertheless, the theory of poroelasticity is effective to explain the observed changes of V_P and V_S in the shallow ground.

On the other hand, the recovery process cannot be explained by the diffusion of water for the following reason. The time constant t_p for change of the excess pore pressure by a diffusion of groundwater is derived from the diffusion eq. (6) of Snieder & van den Beukel (2004) as

$$t_p = \frac{g\rho_w L^2}{\kappa K}, \tag{18}$$

where g, ρ_w, L, κ, K represent gravity acceleration, mass density of water, length scale, bulk modulus of water and hydraulic conductivity of the medium, respectively. Here, we neglect the last term of eq. (6) of Snieder & van den Beukel (2004), which is not important for long lapse times. We assume that water diffuses vertically, which is a 1-D problem. Substituting $g = 9.8$ m s^{-2}, $\rho_w = 10^3$ kg m^{-3}, $L = 12$ m, $\kappa = 2.25\times10^9$ Pa and $K = 10^{-7} \sim 10^{-4}$ m s^{-1} which is typical for clean sands into eq. (18), we obtain $t_p = 6.3 \sim 6.3\times10^3$ s. This time constant is much shorter than the observed time scale of V_S recovery; over a few months at station IBRH16.

In real field conditions, there is also a lateral diffusion of groundwater, which has a time scale of more than a month. However, because the lateral diffusion does not change the net-groundwater level, it cannot explain the V_S recovery observed at most stations (see Fig. 7a).

So far, we argue that a change of pore fluid pressure is responsible for only short-term recovery on a time scale of seconds to hours. The longer recovery process should be more related to healing of cracks in a medium, which corresponds to increase of aspect ratio in eq. (17). It is well known that a shear strength between both sides of the cracks increases as logarithm of the lapse time under a confined normal stress (e.g. Dieterich 1972), thus the recovery of shear modulus may also follow a logarithmic recovery. In laboratory experiments, the logarithmic recovery of a rock sample after a shaking is known as 'slow dynamics', which is a kind of relaxation process inherent in rock (e.g. TenCate *et al.* 2000). This phenomenon is possibly related to long-term recovery observed by our analysis. Also, decompaction after a shaking may affect the long-term recovery because it decreases ϕ. Because K and μ are more sensitive to change of ϕ compared to ρ is (see eq. 17), decompaction increases both V_P and V_S. A laboratory experiment by Knight *et al.* (1995) reports that ϕ increases proportional to logarithm of the number of shaking.

It is likely that the recovery process is governed by multiple factors which have different time scales. This idea is consistent with two-step recovery processes in peak frequency of site amplification factor observed by Wu & Peng (in press). To better understanding of the recovery process, we should apply the V_S, V_P and shear wave splitting analyses to wider range of time scales from seconds to years and carefully examine the transition between the different recovery processes.

6 CONCLUSIONS

We examine time-lapse changes of V_P, V_S and shear wave splitting parameters at depths from 0 to 504 m after the 2011 Tohoku earthquake by applying deconvolution analysis to KiK-net borehole array records. The observed reduction of V_S is up to 6 per cent in the first month after the main shock in large area of northeastern Japan. From the good correlation between the *S*-wave traveltime delay and MDS on the ground surface by the main shock motion, we confirm that the dynamic strain is the main cause of the V_S reduction. Because the correlation with the MDS at the borehole bottom receivers is weak, we speculate that the V_S change is concentrated near the ground surface, probably in loosely packed soil layers. The recovery time of V_S is long if the station is exposed to additional strong motion by aftershocks. The long-term logarithmic recovery cannot be explained by a change of pore fluid pressure, but is more likely to be explained by a recovery of frictional strength of cracks and/or decompaction of the medium. We observe both increase and decrease in V_P, because the net effect of the crack growth and the water saturation in the porous medium does not always reduce V_P. Because the cracks in the shallow subsurface generated by a strong ground motion do not have a specific direction, we do not observe significant changes in the shear wave splitting parameters. Our study provides a basis for monitoring time-lapse changes of multiparameters in the shallow ground including their confidence interval. Because this study examines only shallow part of the ground up to 504 m depth, there is a possibility of changes in the deeper lithosphere as observed by Brenguier *et al.* (2008). Combing the results revealed from this work with the time-lapse changes in the deep lithosphere revealed from repeating earthquakes and ambient noise correlation analyses, we will be able to discuss more about the mechanism of the medium changes associated with a large earthquake.

ACKNOWLEDGMENTS

We are grateful to Dr E. Larose and an anonymous reviewer for their valuable suggestions and comments to improve our paper. We thank NIED for providing us with the KiK-net strong motion records. This study is supported by Japan Society for the Promotion of Science (JSPS grants 22.1224). Seismic Analysis Code (SAC) and Generic Mapping Tools (GMT) are used for signal processing and figure plotting, respectively.

REFERENCES

Alford, R.M., 1986. Shear data in the presence of azimuthal anisotropy: Dilley, Texas, *SEG Expanded Abstr.,* **5,** 476–479.

Asano, Y. *et al.*, 2011. Spatial distribution and focal mechanisms of aftershocks of the 2011 off the Pacific coast of Tohoku Earthquake, *Earth Planets Space,* **63,** 669–673.

Aster, R.C., Borchers, B. & Thurber, C.H., 2011. *Parameter Estimation and Inverse Problems,* Elsevier, Waltham, MA, USA, 260 pp.

Beresnev, I.A. & Wen, K.L., 1996. Nonlinear soil response—A reality? *Bull. seism. Soc. Am.,* **86,** 1964–1978.

Bevington, P.R. & Robinson, D.K., 1992. *Data Reduction and Error Analysis for the Physical Sciences,* McGraw-Hill, New York, USA, 384 pp.

Bhattacharya, S., Hyodo, M., Goda, K., Tazoh, T. & Taylor, C.A., 2011. Liquefaction of soil in the Tokyo Bay area from the 2011 Tohoku (Japan) earthquake, *Soil Dyn. Earthq. Eng.,* **31,** 1618–1628.

Blatt, H., 1979. Diagenetic processes in sandstones, The Society of Economic Paleontologists and Mineralogists (SEPM), Special Publication, **26,** 141–157.

Borcherdt, R.D., 1994. Estimates of site-dependent response spectra for design (methodology and justification), *Earthq. Spectra,* **10**(4), pp. 617–653.

Brenguier, F., Campillo, M., Hadziioannou, C., Shapiro, N.M., Nadeau, R.M. & Larose, E., 2008. Postseismic relaxation along the San Andreas Fault at Parkfield from continuous seismological observations, *Science,* **321**(12), 1478–1481.

Dieterich, J.H., 1972. Time-dependent friction in rocks, *J. geophys. Res.,* **77,** 3690–3697.

Furumura, T., Takemura, S., Noguchi, S., Takemoto, T., Maeda, T., Iwai, K. & Padhy, S., 2011. Strong ground motions from the 2011 off-the Pacific-Coast-of-Tohoku, Japan (Mw = 9.0) earthquake obtained from a dense nationwide seismic network, *Landslides,* **8,** 333–338.

Gardner, G.H.F., Gardner, L.W. & Gregory, A.R., 1974. Formation velocity and density—the diagnostic basics for stratigraphic traps, *Geophysics,* **39,** 770–780.

Gassmann, F., 1951. Elastic waves through a packing of spheres, *Geophysics,* **16,** 673–685.

Gueguen, Y. & Palciauskas, V., 1994. *Introduction to the Physics of Rocks,* Princeton University Press, Princeton, New Jersey, 392 pp.

Hadziioannou, C., Larose, E., Coutant, O., Roux, P. & Campillo, M., 2009. Stability of monitoring weak changes in multiply scattering media with ambient noise correlation: laboratory experiments, *J. acoust. Soc. Am.,* **125,** 3688–3695.

Hobiger, M., Wegler, U., Shiomi, K. & Nakahara, H., 2012. Coseismic and postseismic elastic wave velocity variations caused by the 2008 Iwate-Miyagi Nairiku earthquake, Japan, *J. geophys. Res.,* **117**(B09313), doi:10.1029/2012JB009402.

Koketsu, K. *et al.*, 2011. A unified source model for the 2011 Tohoku earthquake, *Earth planet. Sci. Lett.,* **310**(3–4), 480–487.

Knight, J.B., Fandrich, C.G., Lau, C.N., Jaeger, H.M. & Nagel, S.R., 1995. Density relaxation in a vibrated granular material, *Phys. Rev,* **51,** 3957–3963.

Mehta, K., Snieder, R. & Graizer, V., 2007. Downhole receiver function: a case study, *Bull. seism. Soc. Am.,* **97,** 1396–1403.

Menke, W., 1989. *Geophysical Data Analysis: Discrete Inverse Theory,* Academic Press, Inc, San Diego, CA, USA.

Minato, S., Tsuji, T., Ohmi, S. & Matsuoka, T., 2012. Monitoring seismic velocity change caused by the 2011 Tohoku-oki earthquake using ambient noise records, *Geophys. Res. Lett.,* **39,** L03909.

Nakajima, J., Matsuzawa, T., Hasegawa, A. & Zhao, D., 2001. Three-dimensional structure of V_p, V_s, and V_p/V_s beneath northeastern Japan: implications for arc magmatism and fluids, *J. geophys. Res.,* **106**(B10), 21 843–21 857.

Nakata, N. & Snieder, R., 2011. Near-surface weakening in Japan after the 2011 Tohoku-Oki earthquake, *Geophys. Res. Lett.,* **38,** L17302.

Nakata, N. & Snieder, R., 2012a. Estimating near-surface shear wave velocities in Japan by applying seismic interferometry to KiK-net data, *J. geophys. Res.,* **117,** B01308.

Nakata, N. & Snieder, R., 2012b. Time-lapse change in anisotropy in Japan's near surface after the 2011 Tohoku-Oki earthquake, *Geophys. Res. Lett.,* **39,** L11313.

Obermann, A., Planes, T., Larose, E., Sens-Schonfelder, C. & Campillo, M., in press. Depth sensitivity of seismic coda waves to velocity perturbations in an elastic heterogeneous medium, *Geophys. J. Int.*

Okada, Y., Kasahara, K., Hori, S., Obara, K., Sekiguchi, S., Fujiwara, H. & Yamamoto, A., 2004. Recent progress of seismic observation networks in Japan–Hi-net, F-net, K-net and KiK-net—, *Earth Planets Space,* **56,** 15–28.

Ozawa, S., Nishimura, T., Munekane, H., Suito, H., Kobayashi, T., Tobita, M. & Imakiire, T., 2012. Preceding, coseismic, and postseismic slips of the 2011 Tohoku earthquake, Japan, *J. geophys. Res.,* **117**(B07404), doi:10.1029/2011JB009120.

Rubinstein, J.L. & Beroza, G.C., 2004. Nonlinear strong ground motion in the ML 5.4 Chittenden earthquake: Evidence that preexisting damage increases susceptibility to further damage, *Geophys. Res. Lett.,* **31,** L23614.

Rubinstein, J.L. & Beroza, G.C., 2005. Depth constraints on nonlinear strong ground motion from the 2004 Parkfield earthquake, *Geophys. Res. Lett.,* **32**(L14313), doi:10.1029/2004GL021357.

Sawazaki, K., Sato, H., Nishimura, T. & Nakahara, H., 2009. Time-lapse changes of seismic velocity in the shallow ground caused by strong ground motion shock of the 2000 Western-Tottori earthquake, Japan, as revealed from coda deconvolution analysis, *Bull. seism. Soc. Am.,* **99,** 352–366.

Shiomi, K., Obara, K., Aoi, S. & Kasahara, K., 2003. Estimation on the azimuth of the Hi-net and KiK-net borehole seismometers (in Japanese), *Zisin,* **56,** 99–110.

Silva, B.W., 1976. Body waves in a layered anelastic solid, *Bull. seism. Soc. Am.*, **66,** 1539–1554.

Snieder, R. & van den Beukel, A., 2004. The liquefaction cycle and the role of drainage in liquefaction, *Granular Matter,* **6,** 1–9.

Takagi, R. & Okada, T., 2012. Temporal change in shear velocity and polarization anisotropy related to the 2011 M9.0 Tohoku-Oki earthquake examined using KiK-net vertical array data, *Geophys. Res. Lett.,* **39,** L09310.

Takagi, R., Okada, T., Nakahara, H., Umino, N. & Hasegawa, A., 2012. Coseismic velocity change in and around the focal region of the 2008 Iwate-Miyagi Nairiku earthquake, *J. geophys. Res.,* **117**(B06315), doi:10.1029/2012GL051342.

TenCate, J.A., Smith, E. & Guyer, R.A., 2000. Universal slow dynamics in granular solids, *Phys. Rev. Lett.,* **85**(5), 1020–1023.

Walsh, J.B., 1965. The effect of cracks on the compressibility of rocks, *J. geophys. Res.,* **70,** 381–389.

Wu, C. & Peng, Z., in press. Long-term change of site response after the Mw9.0 Tohoku Earthquake in Japan, *Earth Planets Space*.

APPENDIX A: COVARIANCE MATRIX OF DECONVOLUTION AMPLITUDES

For convenience, we design a bandpass filter with cut-off frequencies f_L and f_H by a Gaussian function

$$W(\omega) = \exp\left[-\left(\frac{|\omega| - \omega_c}{\omega_d}\right)^2\right], \tag{A1}$$

where $\omega_c \equiv \pi (f_H + f_L)$ and $\omega_d \equiv \pi (f_H - f_L)$ are the central angular frequency and the half bandwidth, respectively. This bandpass filter is described in time domain as

$$w(t) = \frac{\omega_d}{2\sqrt{\pi}} \exp\left[-\frac{\omega_d^2}{4} t^2\right] \cos(\omega_C t). \tag{A2}$$

Applying this filter to random data, we obtain the correlation coefficient between the two data samples separated by a discrete time $N\Delta t$ as

$$\frac{w(N\Delta t)}{w(0)} = \exp\left[-\frac{\pi^2}{4} (f_H - f_L)^2 N^2 \Delta t^2\right] \cos[\pi (f_H + f_L) N \Delta t]. \tag{A3}$$

By substituting $N = 1$ and $N = 2$ into eq. (A3), we derive the non-diagonal components of eq. (5).